J. Fluid Mech. (1995), *vol.* 297, *pp.* 1–28

Dynamics and stability of a vortex ring impacting a solid boundary

By J. D. SWEARINGEN†, J. D. CROUCH‡ AND R. A. HANDLER
Naval Research Laboratory, Washington, DC 20375, USA

(Received 22 December 1993 and in revised form 21 October 1994)

Direct numerical simulations were used to study the dynamics of a vortex ring impacting a wall at normal incidence. The boundary layer formed as the ring approaches the wall undergoes separation and roll-up to form a secondary vortex ring. The secondary ring can develop azimuthal instabilities which grow rapidly owing to vortex stretching and tilting in the presence of the mean strain field generated by the primary vortex ring. The stability of the secondary ring was investigated through complementary numerical experiments and stability analysis. Both perturbed and unperturbed evolutions of the secondary ring were simulated at a Reynolds number of about 645, based on the initial primary-ring propagation velocity and ring diameter. The linear evolution of the secondary vortex-ring instability was modelled analytically by making use of a quasi-steady approximation. This allowed a localized stability analysis following Widnall & Sullivan's (1973) earlier treatment of an isolated vortex ring. Amplitude evolution and growth-rate predictions from this analysis are in good agreement with the simulation results. The analysis shows that the secondary vortex ring is unstable to long-wavelength perturbations, even though an isolated ring having similar characteristics would be stable.

1. Introduction

There has been an increasing recognition in the last few decades that organized vortical motions are of great importance in the maintenance of turbulent shear flows. The fundamental dynamics governing the motion of vortex tubes or rings, and their interactions, have been studied extensively as generic models for the more complex behaviour observed in turbulent flows. In particular, the interaction of discrete vortex structures with a boundary has often been used to examine interesting and complex phenomena such as unsteady separation, vortex reconnection, vortex stretching/intensification, vortex instability, and production and dissipation of coherent vorticity. A recent review of these phenomena and how they may be important in applications has been given by Doligalski, Smith & Walker (1994). Other examples of this modelling approach for wall-bounded flows can be found in Acalar & Smith (1987), Walker *et al.* (1987), Chu & Falco (1988), and Lim (1989). A similar approach has been taken to study the interaction of vorticity with a free-surface, both experimentally (Willmarth *et al.* 1989; Bernal & Kwon 1989; and Sarpkaya & Suthon

† Present address: Mechanical Engineering Department, The University of Kansas, Lawrence, KS 66045, USA.
‡ Present address: Boeing Commercial Airplane Group, PO Box 3707, MS 7H-90, Seattle, WA 98124-2207, USA.

1991); and numerically (Dommermuth 1993). The present study considers the evolution of a primary vortex ring as it interacts with a solid boundary to produce a coherent secondary vortex ring. Subsequent three-dimensional deformation of the secondary ring occurs through the evolution of azimuthal instabilities due to its interaction with the primary ring. Previous experimental observations of vortex ring/wall interactions (see for example Walker *et al.* 1987) have given a rather clear qualitative picture of this overall sequence but leave unanswered questions about the nature and physics of the instability process.

This study focuses on the instability of the secondary vortex ring in the presence of the primary ring and a solid boundary. Instabilities of this type can lead to dramatic changes in flow structure and the generation of smaller-scale coherent vortex motions whose vorticity feeds on the parent structure. This reduction in length scale and dispersal of vorticity into the surrounding fluid ultimately results in the dissipation of these structures through the action of viscous diffusion. The phenomena of generation (or regeneration) and dissipation of vorticity are key features of the energy transfer process in turbulent shear flows. Although this model problem cannot necessarily be compared directly to the energetic vortex structures in wall-bounded shear flows, the study of vortices, subsequent instabilities, and their dynamical evolution are nonetheless relevant in a more general sense. Robinson (1989, 1991) has suggested that progress in understanding the dynamics of vortex formation, evolution, and interaction is key to obtaining a fuller understanding of the coherent motions comprising a turbulent boundary layer, and their dynamical role in its maintenance. In this regard, the regenerative properties of the near-wall streamwise-oriented vortices have recently been clearly identified (Smith *et al.* 1991; Falco 1991; Brooke & Hanratty 1993; Bernard, Thomas & Handler 1993).

To investigate the basic instability mechanisms associated with the secondary vortex ring, a complementary approach of numerical experiments and modelling via stability analysis was followed (Swearingen, Crouch & Handler 1991). The interaction of a vortex ring with a wall was directly simulated using three-dimensional fully pseudo-spectral computations (i.e. in all three spatial coordinates); unperturbed and azimuthally perturbed vortex rings were considered. In these simulations an impulsive body force was used to generate the primary vortex ring in much the same manner as it would be formed experimentally. The numerical results are compared to an analytical model for the linear evolution of the instability. The analytical model employed simplifying assumptions that recast the problem into an inviscid analysis for the stability of a vortex ring in close proximity to another vortex ring. The analysis followed the approach used by Widnall & Sullivan (1973) for the long-wavelength stability of an isolated vortex ring. Their results show that isolated thin-core vortex rings are stable to long-wavelength instabilities (over the range of parameters for which the analysis is valid – see Widnall, Bliss & Tsai 1974). The instability normally associated with an isolated ring stems from a short-wavelength mechanism (Widnall *et al.* 1974; Moore & Saffman 1974; Saffman 1978). However, the present analysis shows that when a thin-core vortex ring is in close proximity to another ring, the stability characteristics are altered and long-wave disturbances can grow.

Recently, there have been a number of numerical simulations focusing on the early stages of the interaction of the primary ring with a solid boundary. Orlandi (1990) studied the two-dimensional case and Orlandi & Verzicco (1993) extended this work to the axisymmetric and fully three-dimensional cases. In the work of Orlandi & Verzicco, a finite difference scheme was used to perform axisymmetric simulations of the collision of a vortex ring with a free-slip as well as a no-slip boundary. The axisymmetric

simulations for the no-slip case, performed over a range of ring Reynolds numbers, produced ring trajectories and other flow details which were in reasonable qualitative agreement with the Walker *et al.* (1987) experiments. Differences between simulation and experiment were attributed to three-dimensional effects, absent in the axisymmetric calculations, and differences in the initial ring vorticity distribution.

The fully three-dimensional calculations of Orlandi & Verzicco (1993), which can be most closely compared to the current work, were performed at both low and high resolution for a single Reynolds number. Their simulations were able to reproduce the same kind of instability revealed in the Walker *et al.* (1987) experiments. They find that the ejection of the secondary ring is only slightly affected by the presence of azimuthal instabilities in the primary ring (e.g. the ejection velocity of the secondary ring is greater in the three-dimensional case than that of the axisymmetric case). An important conclusion derived from their work is that the secondary ring is fundamentally more unstable than the primary. This conclusion is based on an analysis of the invariants of the rate-of-strain tensor which reveals that the secondary ring is more sheet-like than the primary and, in addition, there is a greater tendency for vorticity–strain alignment in the secondary ring. However, no attempt was made in Orlandi & Verzicco (1993) to analyse the onset and linear evolution of the secondary-ring instability, an analysis which is presented here in §4.

2. Numerical simulation methodology

2.1. *Solution of the equations of motion*

The accurate simulation of the three-dimensional interaction of a vortex ring with a no-slip wall presented certain numerical issues which required special consideration. A principal issue of obvious concern was the establishment of the vortex ring itself within the computational domain. The ring should be generated sufficiently far from the wall with which it will eventually impact and its radius, core diameter, and initial strength (circulation) should be easily controlled. In this investigation, the stability of the secondary ring generated by the primary ring as it interacted with the wall was of primary concern. Therefore, a method of introducing azimuthally dependent disturbances onto the primary ring was also required.

It is possible to generate a vortex ring with the desired characteristics by specifying an appropriate initial condition for the velocity field which is kinematically consistent with the desired initial vorticity field and is also divergence free. The specification of such a field would present no difficulties in a domain with periodic boundary conditions in all three coordinate directions. In this problem, however, no-slip boundary conditions were needed on at least one wall which, along with the incompressibility constraint, required that both the wall-normal velocity component and its wall-normal derivative be zero at the no-slip wall. A suitable method which satisfied these constraints could not be developed, although it may be possible to generate such an initial condition by using an appropriate combination of image vortices. Experimentally (Sallet & Widmayer 1974), vortex rings are typically generated by a piston stroke which forces a puff of fluid through an orifice. This method has been analysed in detail by Saffman (1975). Implementation of this method would entail addition and removal of mass which would have been numerically cumbersome to implement in the spectral code used here. To avoid these difficulties, a vortex ring was instead generated in a dynamical manner by introducing an appropriate impulsive body force directly into the equations of motion. This method of generating vorticity in two dimensions has been addressed theoretically by Cantwell (1986), and numerically

by Goldstein, Handler & Sirovich (1993) who used body forces to successfully create no-slip surfaces in a spectral code. A complete description of the methodology used to do this is given later in §2.2.

The Navier–Stokes equations were solved in rotational form:

$$\frac{\partial \boldsymbol{V}}{\partial t} = \boldsymbol{V}\times\boldsymbol{\Omega} - \nabla\Pi + \nu\nabla^2\boldsymbol{V} + \boldsymbol{f}, \tag{2.1}$$

where $\boldsymbol{V}$ is the velocity vector, $\boldsymbol{\Omega} = \nabla\times\boldsymbol{V}$ is the vorticity vector, $\Pi = p/\rho + \frac{1}{2}(\boldsymbol{V}\cdot\boldsymbol{V})$, p is the pressure, ρ is the density, ν is the kinematic viscosity, and $\boldsymbol{f}$ is a body force described in detail below. In addition, the incompressibility constraint was enforced:

$$\nabla\cdot\boldsymbol{V} = 0. \tag{2.2}$$

Cartesian coordinates (x, y, z) were used, where x and y are the planar or horizontal coordinates and z is perpendicular to the wall. The corresponding velocity field is (u, v, w), where w denotes the component of velocity in the direction normal to the wall. Here, all variables are non-dimensionalized by a length scale corresponding to the half-height between upper and lower boundaries, and by a unit velocity scale. Note that to obtain alternative scalings, such as that used by Orlandi & Verzicco (1993), the initial vortex ring characteristics could be utilized. For example, the time scale in their simulations is related to the non-dimensional time used in the present study by the factor Γ_0/R_0^2 where Γ_0 is the initial ring circulation and R_0 is its initial radius (see figure 8*a*).

The governing equations were recast in the manner suggested by Orszag & Patera (1981). The final equation system, in which the pressure has been eliminated, consisted of a fourth-order equation for the vertical velocity, w:

$$\left(\frac{\partial\nabla^2}{\partial t} - \nu\nabla^4\right)w = \left(\frac{\partial^2}{\partial x^2} + \frac{\partial^2}{\partial y^2}\right)H_z - \frac{\partial}{\partial z}\left(\frac{\partial}{\partial x}H_x + \frac{\partial}{\partial y}H_y\right), \tag{2.3}$$

and a second-order equation for the vertical vorticity, Ω_z:

$$\left(\frac{\partial}{\partial t} - \nu\nabla^2\right)\Omega_z = \frac{\partial}{\partial y}H_x - \frac{\partial}{\partial x}H_y, \tag{2.4}$$

where
$$H_x = (\boldsymbol{V}\times\boldsymbol{\Omega})_x + f_x, \quad H_y = (\boldsymbol{V}\times\boldsymbol{\Omega})_y + f_y, \quad H_z = (\boldsymbol{V}\times\boldsymbol{\Omega})_z + f_z. \tag{2.5a–c}$$

Following the solution of the equations given above, the streamwise and spanwise velocity components, u and v, were recovered from the incompressibility condition. This method ensured the exact satisfaction of continuity at the end of each time step.

To solve equations (2.3)–(2.5) a spectral spatial discretization of the velocity field was used:

$$V(\boldsymbol{x}, t) = \sum_{k=-K/2}^{K/2-1}\sum_{m=-M/2}^{M/2-1}\sum_{n=0}^{N}\tilde{V}(k, m, n, t)\exp\left[\mathrm{i}(\alpha k x + \beta m y)\right]T_n(z), \tag{2.6}$$

where $\tilde{V}$ are the Fourier–Chebyshev coefficients, $\alpha = 2\pi/L_x$, $\beta = 2\pi/L_y$, L_x and L_y are the domain lengths in the horizontal plane, and T_n are Chebyshev polynomials. For the temporal discretization a Crank–Nicolson scheme was used for the diffusion operator and a second-order Adams–Bashforth scheme was used for the nonlinear terms. The Poisson equations which arise from such a discretization were solved using the tau

method (Gottleib & Orszag 1977). Details of the numerical solution methodology are given in Kim, Moin & Moser (1987). In all simulations the time step was chosen so that the Courant–Friedrichs–Lewy (CFL) number, defined by

$$\mathrm{CFL} = \Delta t \max_{(x,y,z)} \left[\frac{|u|}{\Delta x} + \frac{|v|}{\Delta y} + \frac{|w|}{\Delta z} \right], \tag{2.7}$$

never exceeded 0.2, ensuring numerical stability and time accuracy. The non-dimensional time step utilized for the calculations reported here was $\Delta t = 0.002$. The computational domain used for this study was of size $L_x = L_y = 5$ in the horizontal plane and the height in the normal coordinate direction was $L_z = 2$. A $96 \times 96 \times 65$ computational grid in the x-, y-, and z-directions respectively was used in all of the calculations. This grid size corresponds to the maximum size attainable for the code running on a CRAY XMP/216; as shown subsequently (§2.3) the spatial accuracy achieved using this grid size is adequate. Nominally, the vortex ring with an initial ring diameter of 1 was generated at a distance of 0.5 from the lower boundary of the domain located at $z = -1$. At the boundary nearest the origin of the ring no-slip conditions given by

$$u = v = w = 0 \tag{2.8}$$

were used. Alternatively, the shear-free conditions given by

$$\frac{\partial u}{\partial z} = \frac{\partial v}{\partial z} = w = 0 \tag{2.9}$$

were also used at this boundary. However, the choice of the boundary condition utilized nearest the generation point was not observed to significantly change the formation of the ring or any aspects of its subsequent evolution. The no-slip condition given by (2.8) was used at the wall where the primary ring eventually impacted.

2.2. *Specification of the impulsive force*

The conventional methodology for generating a single vortex ring experimentally is to eject a puff of fluid through a circular sharp-edged orifice or nozzle. The cylinder slug of fluid that emerges eventually rolls up into a propagating vortex ring of total circulation Γ, radius R, and core size a. In the simplest manner, this initiation of a vortex ring is often idealized as being produced by a circular disk of radius R which is suddenly moved normal to its plane and then brought to rest again. The details of the formation process have been considered in a number of studies and the reader is referred to Magarvey & MacLatchy (1964*a*), Maxworthy (1972), Sallet & Widmayer (1974), and Saffman (1975); discussion of vortex ring generation in terms of an impulsive force applied over a circular area is also given in the text by McCormack & Crane (1973). Analogously, this study used an impulsive body force applied to a cylindrical region of fluid to generate a vortex ring with the desired properties. The impulsive body force introduced directly into the equations of motion was of the form

$$f_z(r, \theta, z, t) = \mathscr{A}\mathscr{T}(t)\mathscr{F}(z)\mathscr{H}(r, \theta). \tag{2.10}$$

Here r and θ specify a cylindrical coordinate system (for ease of formulation) that can be related to the Cartesian coordinates of the original computational domain by

$$r = [(x-x_0)^2 + (y-y_0)^2]^{1/2} \quad \text{and} \quad \theta = \tan^{-1}\left(\frac{y-y_0}{x-x_0}\right), \tag{2.11}$$

where the point (x_0, y_0) gives the location in the horizontal plane where the body force application was centred. Only the wall-normal component of the force, f_z, was specified since it was desired to generate a ring at normal incidence to a wall in a specified (x, y)-plane (i.e. $f_x = f_y = 0$). Note that the other body force components could be specified in an appropriate way so that rings of any desired incidence to the solid boundary would be produced. This has been done and the study of the ring interaction with an inclined wall will be reported elsewhere (see Lim 1989 for an experimental description of this interaction).

In (2.10), $\mathscr{A}$ is an amplitude constant which was adjusted to obtain a ring of the desired circulation strength; the time-dependent function $\mathscr{T}(t)$ was used to ensure that the impulsive force was applied smoothly in time and that it decayed to zero amplitude soon after the ring was generated. This time window function was taken in the following form:

$$\mathscr{T}(t) = \tfrac{1}{2}[1 + \tanh \alpha(\tau - t')], \tag{2.12a}$$

where

$$t'(t) = [(t - t_0)^2]^{1/2} \tag{2.12b}$$

and t_0 prescribed the location in time at which the window function was applied, τ specified the duration of the time window, and α the 'smoothness' with which the window was applied. (Note that $\alpha = \infty$ would correspond to a rectangular window function with step discontinuities at $t = t_0 \pm \tau$). A plot of this time window function is shown in figure 1 (*a*). The time-dependent introduction of the body force prescribed by this function was always applied at the beginning of the calculation, normally with $t_0 = 0.05$, and served to eliminate discontinuities at the beginning and end of the impulsive force introduction. Similar in shape to the time window function $\mathscr{T}(t)$, $\mathscr{F}(z)$ was a tapered window function (spatial) used to confine the impulsive force to a cylindrical region with small extent in the wall-normal direction:

$$\mathscr{F}(z) = \tfrac{1}{2}[1 + \tanh \beta(B_z - z')], \tag{2.13a}$$

where

$$z'(z) = [(z - z_0)^2]^{1/2} \tag{2.13b}$$

and z_0 was the point in the normal direction where the impulsive force distribution was centred, B_z determined the axial length of the cylindrical region over which the impulsive force was applied, and β prescribed the smoothness of the spatial tapering in this direction. Using the analogy to the experimental generation of a vortex ring, function $\mathscr{F}(z)$ essentially defined the axial length (here nominally of extent $\approx z_0 \pm 0.1$) of the cylindrical fluid slug emerging from the orifice to form the ring.

Function $\mathscr{H}(r, \theta)$ was a superposition of several other functions and was used to obtain a ring with the desired vorticity profile, ring diameter, and core diameter and to allow the addition of azimuthally dependent disturbances. This function took the form

$$\mathscr{H}(r, \theta) = h_1(r) + h_2(r) \sum_{n=1}^{N} \epsilon_n \cos(n\theta + \phi_n), \tag{2.14a}$$

where

$$h_1(r) = \tfrac{1}{2}[1 + \tanh \gamma(C_r - r)] \tag{2.14b}$$

specified an approximately cylindrical region of radius C_r, across which the impulsively applied force was constant (i.e. analogously, the cross-section of the fluid slug); outside this region the force was zero (C_r approximately determined the eventual radius R of the generated vortex ring). The tanh profile provided a smooth transition between these two regions; the parameter γ determined the extent of this transition region and thus

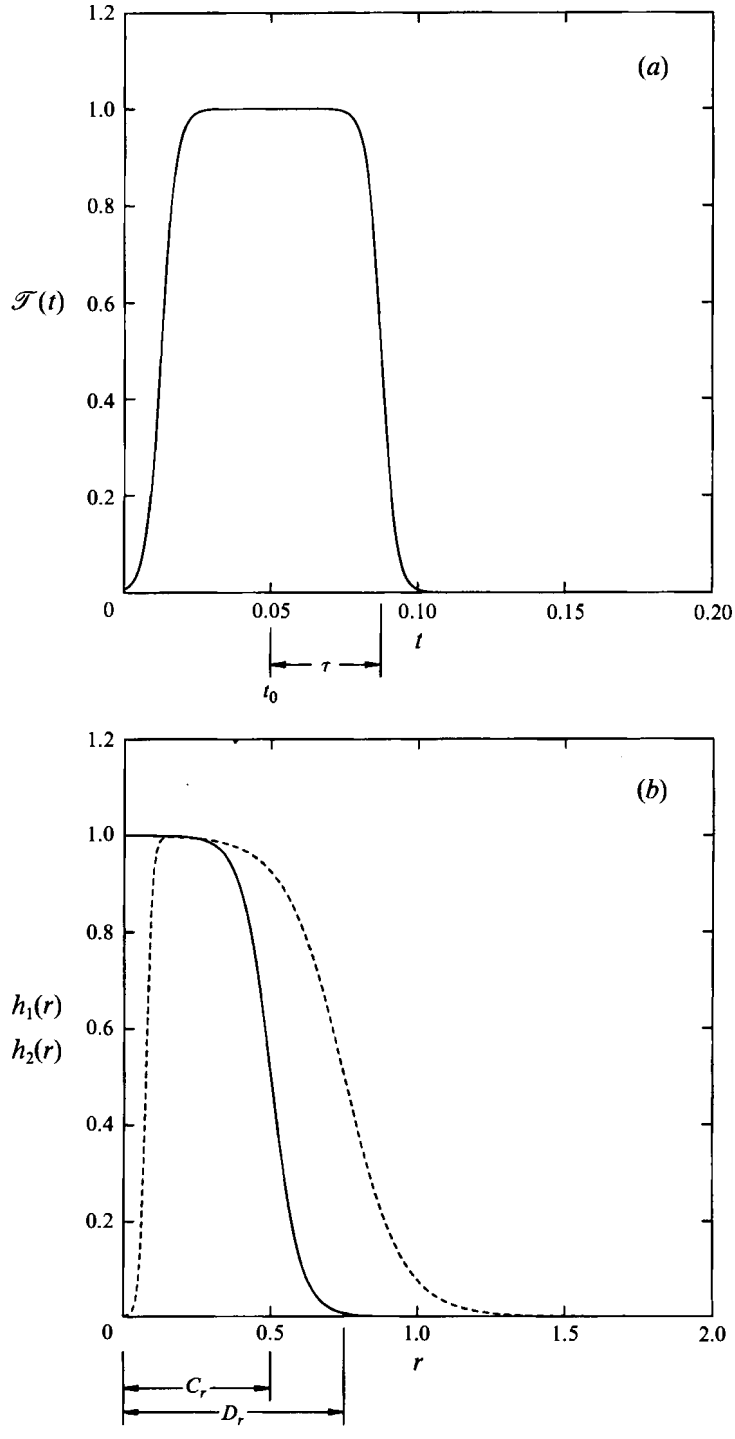

FIGURE 1. Windowing functions used in prescribing the form of the impulsively applied body force for the primary ring generation. (*a*) Time windowing function $\mathscr{T}(t)$; (*b*) functions $h_1(r)$ (——) and $h_2(r)$ (– – –) used to prescribe the primary ring characteristics and disturbance location.

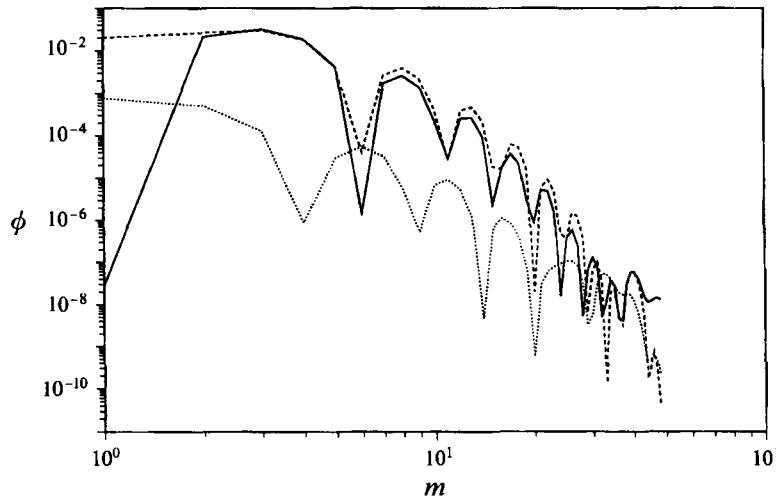

FIGURE 2. Wavenumber (k_y) spectra for a ring with a mode-6 disturbance at $t = 1.8$. The spectrum, ϕ, is defined as $|a_n|^2$, where the a_n are the complex Fourier amplitudes. The wavenumber axis is the wavenumber index m ($k_m = \beta(m-1)$ for $m = 1, M/2$, equation (2.6)). ·····, u; ——, v; – – –, w.

the approximate vortex-ring-core diameter. The second term in equation (2.14*a*) provided for the superposition of a small disturbance on the basic impulsive force distribution provided by function $h_1(r)$. Function $h_2(r)$ was constructed to isolate the applied disturbance only to the core region of the vortex ring eventually generated:

$$h_2(r) = \{\tfrac{1}{2}[1+\tanh\delta(D_r-r)]\}\{\tfrac{1}{2}[1+\tanh\eta(r-E_r)]\}. \tag{2.14c}$$

Parameters δ, η, D_r, E_r could be adjusted to control where the disturbance was introduced with respect to the primary force distribution. Functions $h_1(r)$ and $h_2(r)$ are shown in figure 1(*b*). The parameters ϵ_n and ϕ_n are the amplitude and random phase respectively of individual azimuthal modes. The specification of the body force described by (2.10)–(2.14) allowed the introduction of any desired azimuthal disturbance to the primary vortex ring.

Although vortex rings of widely varying characteristics could be generated using the methodology described by (2.10)–(2.14), no attempt was made to exhaustively study the generation process. Rather, the vortex rings generated were prescribed to approximately match those observed in the experimental work of Walker *et al.* (1987) as discussed below in §3. Qualitatively, however, it was found that the vortex ring circulation and propagation velocity could be adjusted by changing either the amplitude constant $\mathscr{A}$ or the total length of time over which the impulsive force was applied (approximately 2τ).

2.3. *Spatial accuracy*

To determine the spatial accuracy (convergence) of the simulations, wavenumber spectra for the velocity field were computed. The spectra were obtained by taking the Fourier transform of each velocity component from a simulation of a perturbed primary ring (see case ii described in §3.) The results shown in figure 2 were obtained at an instant in time ($t = 1.8$, refer to figures 5 and 7) for which the primary ring was sufficiently far from the wall so that a secondary ring had not yet formed. The spectra in the spanwise y-direction (k_y spectra) shown in figure 2 were obtained from the velocity field $V(x_0, y, z_0)$; the coordinate x_0 was set to $L_x/2$, the centre of the ring, and

z_0, the wall-normal coordinate, was chosen such that the y-component of velocity (root-mean-square value), v, was a maximum (i.e. spectra along a line in the horizontal plane of the ring but below the centre of the vortex cores). The results show spectra exhibiting lobes, or local maxima, which can all be related to the two dominant length scales, the ring and core diameters, and their harmonics. It is evident that the dynamic range of the calculation (ratio of the maximum spectral energy to the lowest) is six to nine orders of magnitude and there is no evidence of any energy pile-up at high wavenumbers. Thus, the grid-scale velocity amplitudes are 10^3–10^4 times smaller than the energy-containing low-wavenumber modes, indicating sufficient accuracy for the purposes of our work. Chebyshev spectra (z-direction) were also obtained and show approximately the same spectral decay. It should be noted that in high-resolution calculations of fully developed channel flow turbulence (Kim *et al.* 1987) the dynamic range in spectral energy was never more than seven orders of magnitude.

3. Numerical simulation results

A laminar vortex ring was generated and allowed to propagate unimpeded through quiescent fluid before interacting with the solid boundary. The initial primary ring can be characterized by its Reynolds number $Re_0 = V_0 D_0/\nu$, based on the initial propagation velocity V_0, the initial ring diameter D_0, and the kinematic viscosity ν. Walker *et al.* (1987) observed that primary rings with Re_0 in the range 600–1300 lead to similar qualitative flow behaviour. Thus only representative cases at $Re_0 \approx 645$ are discussed here. Typically, the ring diameter was chosen to be $D_0 = 1$ relative to the 5×5 domain size in the horizontal plane. These are non-dimensionalized based on the characteristic length defined by half the normal coordinate distance between two horizontal bounding surfaces (one of these would be the solid boundary where the ring interaction eventually took place). Nominally, these horizontal bounding surfaces were located at $z = \pm 1.0$. A schematic detailing the computational domain and the various parameters defining the vortex-ring characteristics is given in figure 3. For clarity only one-half of the vortex ring is sketched, but the simulations utilized a complete and fully three-dimensional vortex ring. The large size of the domain in the horizontal plane relative to the vortex-ring diameter allowed for the eventual increase in ring diameter during the wall interaction process without significant periodic-domain end effects. The primary-ring core was relatively thin with an initial-core radius to ring-radius ratio of approximately 0.2.

Two simulations at the chosen Re_0 are discussed: (i) unperturbed and (ii) perturbed. In the perturbed case, disturbances were introduced into the coherent secondary ring generated during the primary ring/wall interaction process. More specifically, disturbances of the form prescribed by (2.14*a*) were superimposed on the primary ring during the generation process at the beginning of the calculation and these subsequently were imparted to the secondary ring. In both unperturbed and perturbed cases the disturbance field prescribed contained a spectrum of thirty modes (i.e. $N = 30$ in (2.14*a*)) with each mode given a randomly chosen phase ϕ_n. The two cases then differed only in terms of the relative amplitudes ϵ_n set for each mode contained in the spectrum of the disturbance field. No significant distortion of the secondary vorticity was observed (i.e. the unperturbed case) when the disturbance field contained the background spectrum of azimuthal modes at amplitudes $\epsilon_n = 10^{-5}$ relative to the overall initial strength of the primary ring. Unstable evolution of a selected mode (i.e. perturbed case) was observed when its amplitude was increased to $\epsilon_n \approx 10^{-2}$ above the background spectrum amplitude. Here, detailed results for the evolution of a

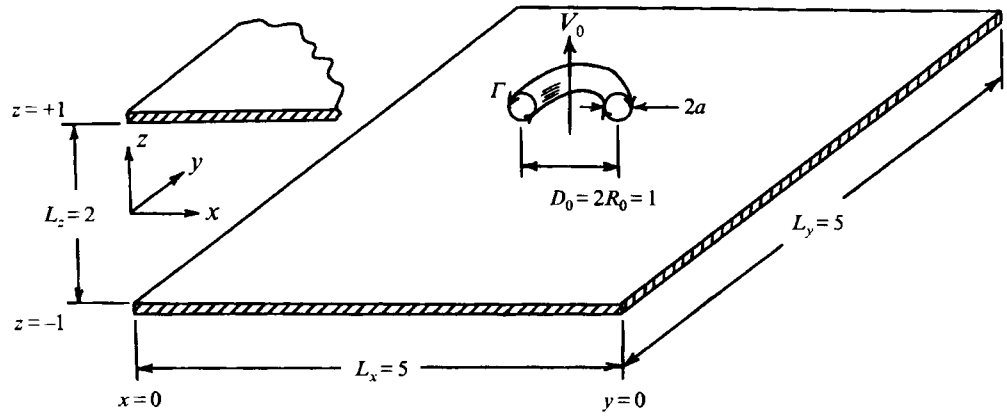

FIGURE 3. Schematic of a vortex ring located in the computational domain.

disturbance with six wavelengths ($n = 6$ in (2.14a)) around the ring are presented. A mode $n = 6$ azimuthal disturbance was chosen for discussion because it is the maximum wavenumber for which the long-wavelength approximation used in the analytical work remains 'fully valid' (see §4). Other wavenumber disturbances were considered (single mode $n = 3$ and modes $n = 3, 6$ in combination), but the results for these simulations are well represented by the results presented here for $n = 6$. For each simulation, sixty three-dimensional realizations of the flow separated by $\Delta t = 0.1$ were stored for further analysis. Example perspective views of the vortex ring development at $t = 4.1$ for both the unperturbed and perturbed cases are shown in figure 4. Here surfaces of constant vorticity magnitude are plotted in three dimensions as cutaway views (i.e. in only half of the computational domain) so that the vortex cores can easily be discerned. Superimposed on the constant-vorticity surfaces in the plane of the cut (an (x, z)-plane) are coloured contours of constant Ω_y vorticity with positive vorticity shown as shades of red/yellow and negative as blue/green. The primary ring (distinguished as the blue/green core on the left-hand side of each realization) has interacted with the solid boundary to produce a coherent secondary vortex ring (distinguished as the core interior to the primary ring but coloured red/yellow on the left). The realization in figure 4(a) shows the unperturbed case; the low-amplitude background spectrum of disturbances initially introduced has not produced an unstable evolution of the secondary ring. Conversely the realization for the perturbed case of figure 4(b) where the $n = 6$ mode amplitude was introduced at a higher level than the background spectrum of disturbances shows an unstable evolution. This is evidenced by the significant azimuthal distortion in the secondary ring. It is observed that both the perturbed and unperturbed cases evolve in exactly the same manner until the point ($t \approx 3.2$) when the $n = 6$ mode disturbance has grown significantly. It is worth noting here that the evolution of the instability in the secondary ring is reasonably well resolved in these simulations; approximately 17 grid points are contained in one wavelength of the $n = 6$ mode disturbance.

The temporal evolution of the primary vortex ring and the secondary vorticity field it generates on approach to the no-slip boundary is shown in figure 5. Contours of constant vorticity (Ω_y for this view) on the (x, y)-plane of symmetry are plotted at six discrete time steps for the perturbed case (ii) with a mode $n = 6$ azimuthal disturbance. In this figure, the solid boundary is at $z = +1$ and only a portion of the entire plane is shown for clarity. When the primary ring is approximately two ring radii from the

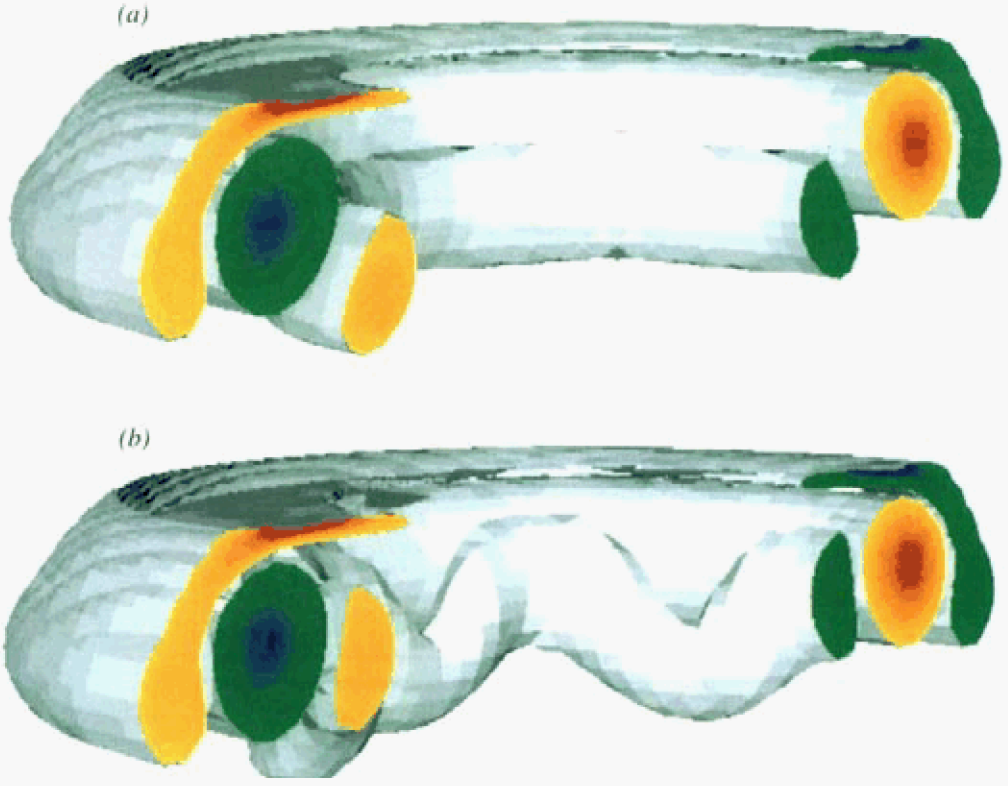

FIGURE 4. Perspective view of the vortex ring/wall interaction (*a*) without, and (*b*) with an azimuthal mode-6 perturbation at $t = 4.1$. Surfaces are of constant vorticity magnitude $|\boldsymbol{\Omega}| = 3.0$. Coloured regions show constant contours of Ω_y; green to blue (-3.2 to -34.9); yellow to red ($+3.2$ to $+34.9$). In each realization, the wall is located at the top of the domain shown.

solid surface, a boundary layer is formed adjacent to the wall as a natural consequence of the no-slip condition at the boundary and the radial flow induced by the ring.

The radius of the ring increases as it approaches the wall in agreement with inviscid theory. This is accompanied by a commensurate decrease in the core size. Unsteady separation of the boundary layer formed on the wall arrests further radial growth of the primary rings and ultimately leads to the ejection of a coherent secondary vortex ring of opposite rotation. An examination of the pressure field at the wall (not given here) showed that the pressure increases with increasing radial distance from the centre of the primary ring core where the pressure is a minimum. This adverse radial pressure gradient is the cause of the separation of the wall boundary layer as discussed in Walker *et al.* (1987). The detachment of vorticity from the wall is associated with the rebounding of the primary vortex ring away from the wall. The sheet of detached vorticity azimuthally surrounds the primary ring. Further evolution of this process produces an elongated region of concentrated secondary vorticity which subsequently pinches off to form a coherent axially symmetric secondary vortex ring. Assuming sufficient initial strength in the primary ring, the process will be repeated to form a another ring, and at $t = 4.4$ it is evident that the separated boundary-layer vorticity is just beginning its coalescence into such a tertiary ring.

Once formed, the secondary ring propagates around the primary ring under the

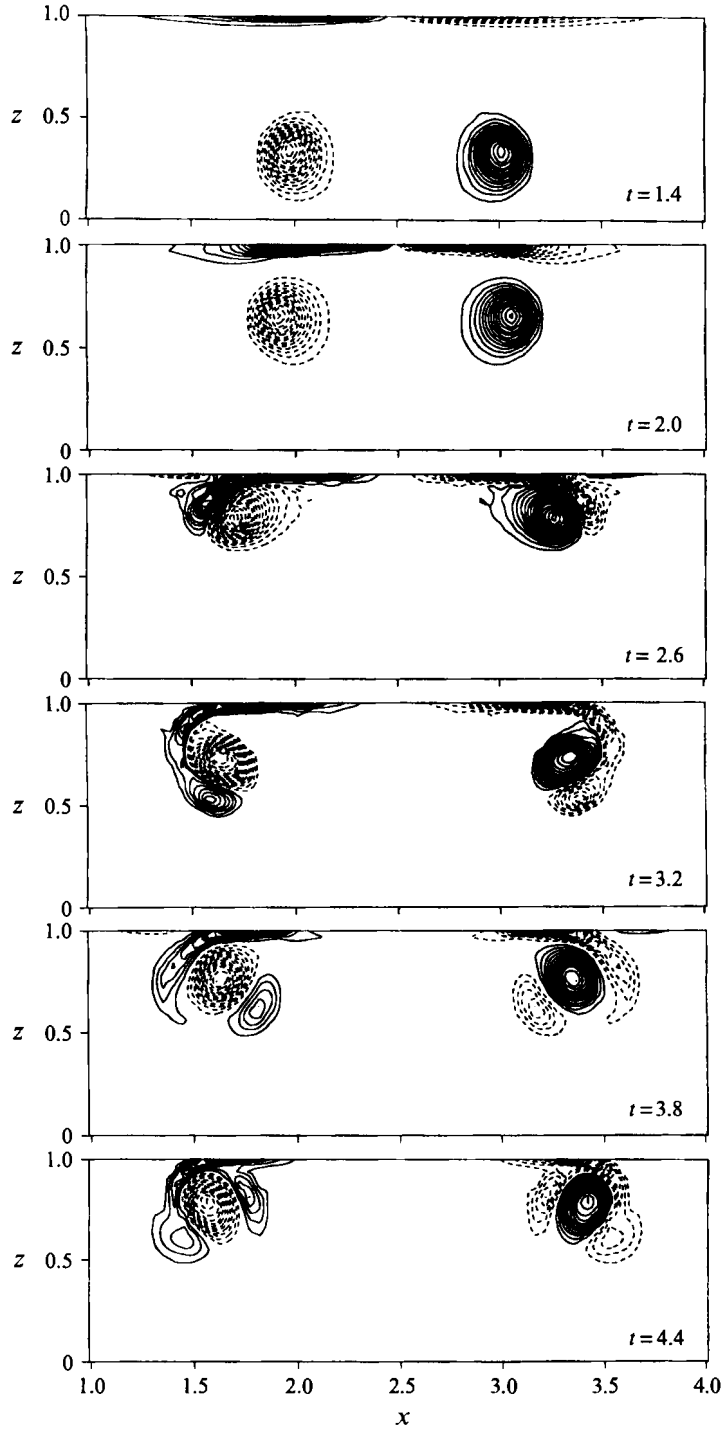

FIGURE 5. Temporal evolution of the primary and secondary rings. Contours are of constant vorticity (Ω_y) and the wall is at $z = 1.0$. Negative vorticity contours are shown as dashed lines.

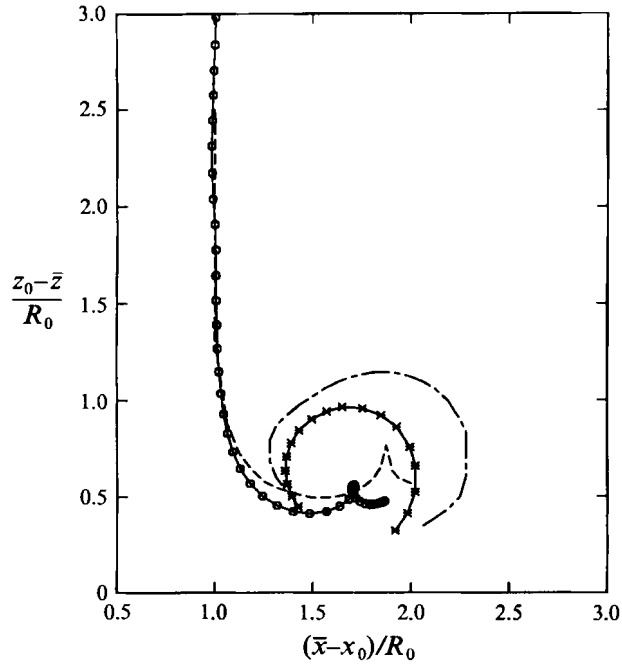

FIGURE 6. Trajectories of the primary and secondary rings. Simulation, $Re_0 \approx 645$: ○, primary; (*), secondary; ●, location corresponding to the origin of the secondary-ring trajectory. Experiments (Walker *et al.* 1987), $Re_0 = 564$: – – –, primary; ——, secondary. The time step between data points is $\Delta t = 0.1$.

combined influence of the primary- and secondary-ring circulations (Biot–Savart effects). Meanwhile, the position of the primary ring remains relatively fixed. During this mutual interaction, the secondary-ring core is continually sheared by the primary ring giving the secondary core a near-elliptic cross-section. In the absence of any growing azimuthal perturbation (case i), the secondary ring simply progresses over the top of the primary ring and then down through the centre where it merges with the still-existing wall boundary-layer vorticity. Subsequent re-ejection can occur if the primary ring still maintains sufficient energy. Although not shown in the evolution of figure 5, the rather weak tertiary ring behaves in a similar way to the secondary ring, but it does not significantly influence the motions of the secondary ring. The events described here are qualitatively similar to those observed in some detail in previous experimental efforts (Magarvey & MacLatchy 1964*b*; Yamada & Matsui 1982; Walker *et al.* 1987), providing validation that the numerical simulations faithfully reproduced the flow behaviour.

A comparison between the experimental results of Walker *et al.* (1987), for which $Re_0 = 564$, and the numerical simulation results of the present study is given in figure 6. The trajectories of the vortex-ring cores in the (x, z)-plane of symmetry are shown for the mode $n = 6$ disturbance case. The location of a vortex core at any instant in time is given by the centre of vorticity denoted by its location above the wall, $\bar{z}$, and its distance from the centre of the ring, $\bar{x}$. The centre of vorticity (i.e. the first moment of the vorticity distribution) is defined by

$$\bar{x} = \frac{1}{\Gamma}\int_A x\Omega_y \,\mathrm{d}x\,\mathrm{d}z, \quad \bar{z} = \frac{1}{\Gamma}\int_A z\Omega_y \,\mathrm{d}x\,\mathrm{d}z, \tag{3.1}$$

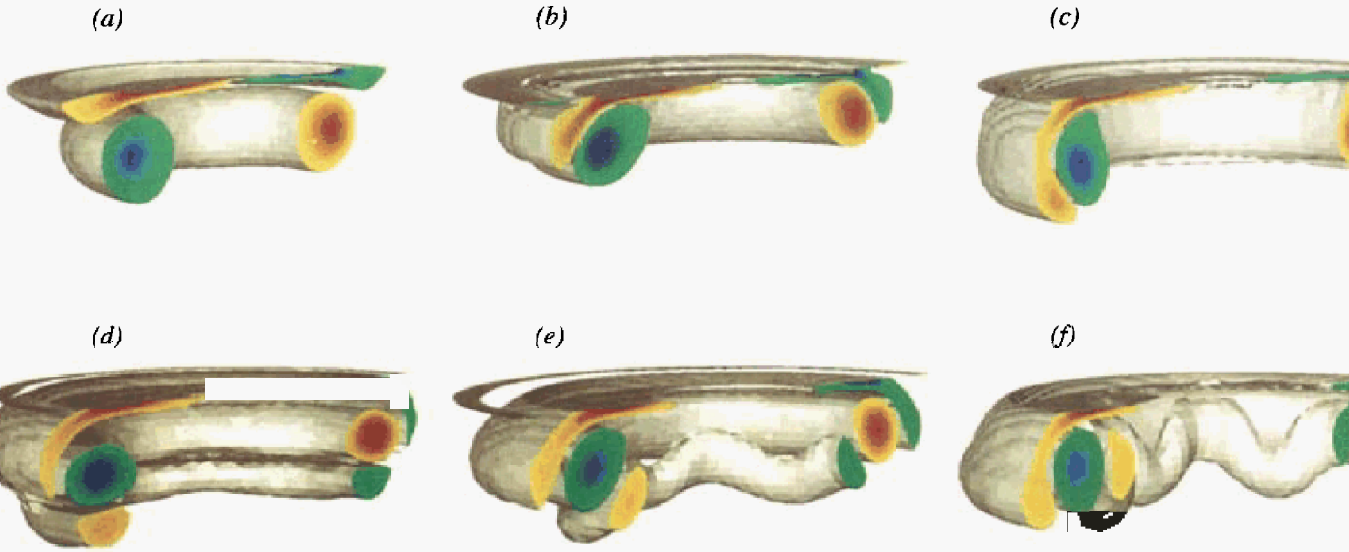

GURE 7. Perspective views of a vortex ring impinging on a wall with a mode-6 azimuthal disturbance present. Surfaces are of constant agnitude $|\boldsymbol{\Omega}| = 3.0$. Coloured regions show constant contours of Ω_y; green to blue (-3.2 to -34.9); yellow to red ($+3.2$ to $+34.9$). (*a*)) $t = 2.6$, (*c*) $t = 3.0$, (*d*) $t = 3.4$, (*e*) $t = 3.8$, (*f*) $= 4.2$.

where Ω_y is the spanwise vorticity, A is the region over which $\Omega_y \geqslant k\Omega_{max}$, and Γ is the vortex-core circulation given by

$$\Gamma = \int_A \Omega_y \, \mathrm{d}x \, \mathrm{d}z. \tag{3.2}$$

At a particular time instant, Ω_{max} specifies the peak vorticity magnitude of the vortex core under consideration and the threshold level k determines the closed contour in the (x, z)-plane which defines the vortex-core cross-section. Threshold values in the range 0.00625 to 0.20 were examined. The choice of a particular value in this range was driven by the need to select a contour which would include as much of the ring vorticity as possible (i.e. largest A) yet which would define a finite domain for the ring. To best balance these conflicting considerations, a threshold value of $k = 0.0375$ was somewhat arbitrarily selected for use in all subsequent calculations. From the parameter study, it was found that when this value of k was changed by a factor of two the results (core location and circulation) varied by less than 5%. To facilitate the comparison in figure 6, the trajectories are scaled by the initial primary ring radius R_0 and translated so that the virtual origin (x_0, z_0) is located on the primary-ring axis of symmetry ($x = L_x/2$) at the solid boundary ($z = +1$). The time step between data points is $\Delta t = 0.1$. Primary- and secondary-ring trajectories from the simulation results are similar to those of the experimental work. The primary-ring diameter increases by a factor of approximately two. As in Walker *et al.* (1987), the point on the primary-ring trajectory corresponding to the origin of the secondary-ring trajectory is noted. The generation of secondary vorticity is responsible for the arrested radial spreading of the primary ring and the eventual rebound of the primary ring away from the wall. The obvious discrepancies between the simulation and experimental trajectories are attributed to differing values of Re_0 and the 'fatter' vortex cores generated in the experiments.

The time sequence of three-dimensional views of the primary-ring interaction with the boundary given in figure 7 shows the growth of an azimuthal mode-6 disturbance on the secondary vortex ring over the period $2.2 \leqslant t \leqslant 4.2$. Here the perspective views are presented in the same way as those shown previously in figure 4 (i.e. surfaces of constant vorticity magnitude along with positive and negative coloured vorticity contours on the plane cut through the field). The generation and evolution of the secondary ring happens in the same manner as for the unperturbed case up until $t \approx 3.2$ where the disturbance has grown significantly and becomes visually apparent (it will be shown subsequently that the disturbance has in fact grown substantially prior to this time). As the secondary ring propagates around the primary ring and is eventually compressed by passing through its centre towards the wall, the disturbance continually grows, resulting in the loop structure observed by Walker *et al.* (1987).

To facilitate a comparison with the analytical model of the secondary-ring instability described in §4, it is necessary to characterize the vortex cores for the perturbed case (ii) in terms of the circulation Γ, as defined above, and the vortex-core radius a. At a particular time instant, the circulation was found by integrating the vorticity over the area A enclosed by the contour defined by $k = 0.0375$. Similarly, the vortex-core radius was defined as the radius of gyration about the centre of vorticity specified by $(\bar{x}, \bar{z})$; this second moment of the vorticity distribution over region A is then given by

$$a = \frac{1}{\Gamma^{1/2}} \left[\int_A \{(x-\bar{x})^2 + (z-\bar{z})^2\} \, \Omega_y \, \mathrm{d}x \, \mathrm{d}z \right]^{1/2}. \tag{3.3}$$

Figures 8(*a*) and 8(*b*) respectively show the vortex-core circulation (scaled with R_0^2) and the non-dimensional core radius a/R_0 as a function of time for both the primary and

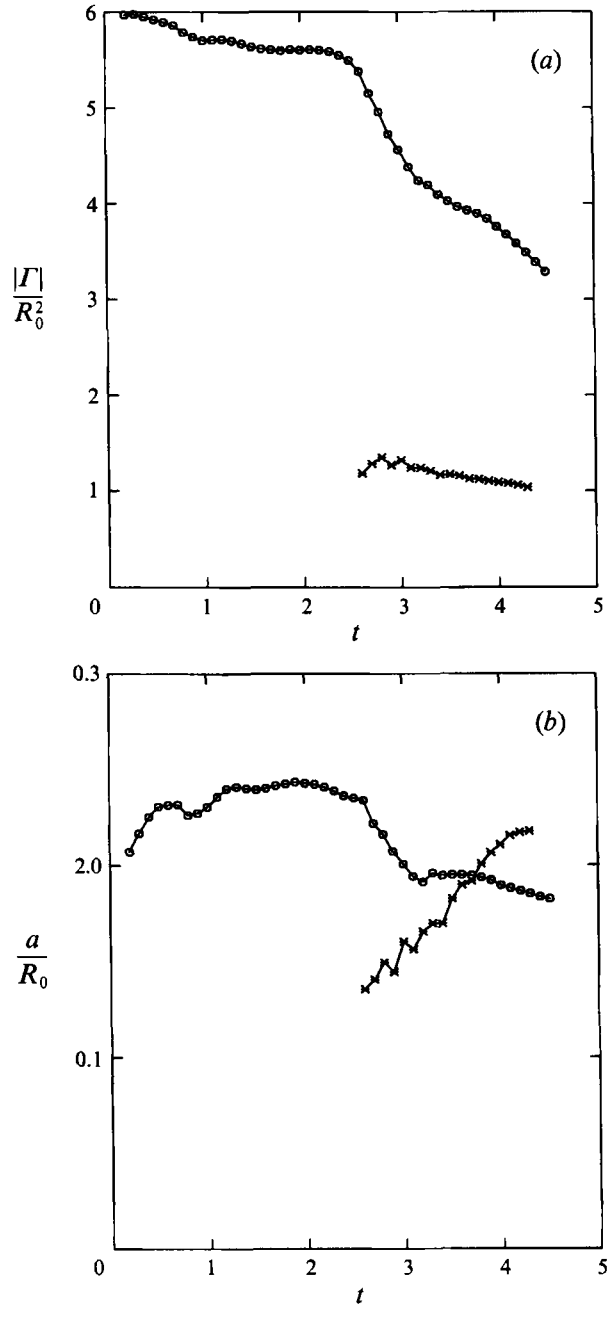

FIGURE 8. Properties of the primary (○) and secondary (*) rings: (*a*) circulation magnitude; (*b*) core radius.

secondary vortex rings. Note that the circulation magnitude has been plotted since the primary and secondary vortex cores have opposite signs of circulation corresponding to their opposite senses of rotation. During the lifetime of the secondary vortex ring ($2.8 \leqslant t \leqslant 4.3$), the circulations of both the secondary and primary rings decrease by approximately 25%. For $t \geqslant 3.0$ the ratio of the magnitudes of the primary- and

secondary-ring circulations remains almost constant (less than 5% variation) at a value of $|\Gamma_1|/|\Gamma_2| \approx 3.5$. During this same time period ($2.8 \leqslant t \leqslant 4.3$), the size of the secondary core increases by 40% and the primary-ring-core size decreases by approximately 15%. This observation agrees with the evidence presented in figure 5 showing vorticity contours in the cross-stream plane as a function of time.

The onset and evolution of instabilities developed in the secondary ring are now examined. The trajectory determination based on vorticity centroids serves as a useful starting point to analyse the secondary-ring development when azimuthal instabilities are present. For azimuthally undeformed cores (like the primary-ring core or the unperturbed secondary core), application of (3.1) at any plane of symmetry placed through a core unambiguously defines the location of its centre. However, application of this definition to the unstable (case ii) three-dimensionally deformed secondary vortex cores is not necessarily an efficient or straightforward procedure. Instead, the instantaneous position of the secondary-ring core was ascertained using (3.1) for a single plane intersecting the ring axis. This position was then used as a convenient starting point for a subsequent determination of a vortex line passing circumferentially through the secondary-ring core. Vortex lines were determined by using the definition, $\mathrm{d}\boldsymbol{x}/\mathrm{d}s = \boldsymbol{\Omega}/|\boldsymbol{\Omega}|$ where s is the distance along the vortex line and $\boldsymbol{x}$ is the vector drawn to any point on the line. Using the full three-dimensional flow field at a given instant in time and starting from the initial location $\boldsymbol{x}_0$ provided by (3.1), the vortex lines were obtained by numerically integrating the definition given above. Care must be exercised when using vortex lines to infer the behaviour of coherent lumps of vorticity, since the particular vortex line traced depends on the chosen starting location (see for example Robinson 1989). Here the starting location clearly resides on the interior of the secondary-ring core and thus the vortex line can be expected to remain there and properly terminate on itself.

When significant azimuthal perturbations are present (case ii above), the temporal development of instabilities in the secondary ring can be studied quantitatively by observing the evolution of the vortex lines determined from the procedure defined above. Again note that the same basic sequence of events as given in figure 5 is followed for both the unperturbed and perturbed cases up to $t \approx 3.2$. Until this time, very little visual evidence of a growing disturbance is apparent. This behaviour is demonstrated clearly in figure 9 which shows a sequence of vortex-line images determined in the manner discussed previously for the secondary ring during the growth of an azimuthal (mode-6) disturbance. Changes in the mean radius of the ring result from its progression around and over the primary ring. The disturbance present in the secondary ring undergoes a rapid growth for the time period between $t = 3.2$ and 4.3, while over this same period the mean length scales (ring radius and core radius – see figures 6 and 8*b*) of both primary and secondary rings have changed relatively little (at most 30%). The deformations in the secondary ring become comparable to its mean size as it progresses over the top of the primary ring, becoming compressed by its passage through the primary-ring centre. The behaviour here is qualitatively different from the unperturbed case since only some portions of the secondary ring migrate close enough to the boundary to merge with the wall layer. These lower portions of the deformed secondary ring actually pass beneath and around the primary-ring core, while the upper ends of the secondary ring remain removed from the wall as it is progressively stretched. Cerra & Smith (1983) observed this same behaviour and found that this deformed loop structure is maintained to Reynolds numbers up to approximately 1600 where the onset of another type of evolution is observed which involves a complex interaction with the tertiary vortex ring. The instability evolution

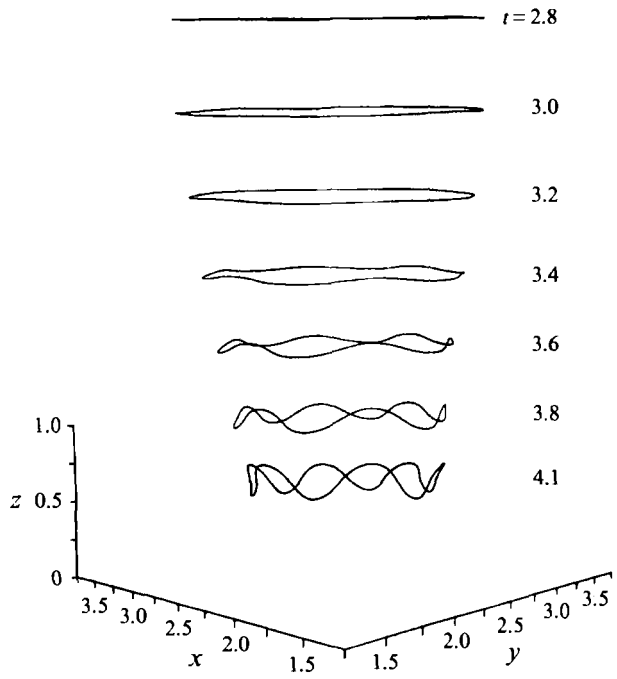

FIGURE 9. Temporal evolution of the instability of the secondary ring. Vortex lines defining the secondary ring are shown.

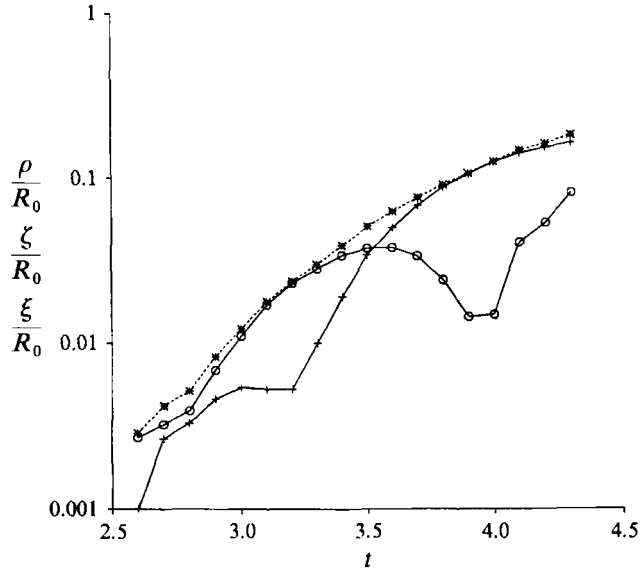

FIGURE 10. Evolution of the secondary-ring instability amplitudes $\rho(\bigcirc)$ and $\zeta(+)$ from the numerical simulation at $Re_0 \approx 645$. The total perturbation amplitude $\xi(*)$ is also shown.

observed here occurs on a much faster time scale than the mean motion of the secondary ring. Meanwhile, the primary-ring position remains essentially fixed.

By analysing the secondary-ring evolution in the manner presented in figure 9, the amplitude evolution of the developing instability can easily be ascertained. For this

purpose the amplitudes ρ and ζ are respectively defined to be the radial and axial components of the azimuthal perturbation to the secondary ring. These amplitudes were determined by azimuthally averaging the core deformations at a given instant in time. The arithmetic mean over the interval $[0, 2\pi]$ defines the mean position of the secondary core, whereas the variance about this mean defines the perturbation amplitudes. A total perturbation is defined as the modulus of these two, $\xi = (\rho^2 + \zeta^2)^{1/2}$. Figure 10 shows the amplitude evolutions calculated in this manner and scaled by R_0. Initially the radial perturbation ρ grows while the axial perturbation ζ is slightly damped. This is subsequently followed by rapid growth in the axial component and the eventual decay of the radial component. The total perturbation ξ grows continuously over this time period. Note that even for the period $2.6 \leqslant t \leqslant 3.2$ when the growth of the disturbance is not visually apparent as in figures 7 and 9, a substantial increase in the disturbance amplitude takes place (approximately by a factor of 8). Over the entire evolution presented for $2.6 \leqslant t \leqslant 4.3$ the total perturbation increases by a factor of approximately 65.

4. Analytical model for secondary-ring instability

The numerical simulations provide a framework for studying the sequence of processes associated with the vortex ring impinging on a solid boundary. This sequence involves the formation and evolution of a secondary vortex ring as discussed in §3. The evolution of the secondary ring when weak perturbations are present in the flow is now examined. In particular, an analytical model for the onset and linear evolution of the azimuthal secondary-ring instabilities was developed.

4.1. *Formulation of stability problem*

The dynamics of the secondary vortex ring during the early development of instability can be characterized by two distinct time scales. After the formation of the secondary ring, the primary-ring size and position remain almost constant. Therefore, the primary-ring motion is neglected in the analysis. As the secondary ring propagates slowly around the primary ring, azimuthal perturbations develop and grow rapidly leading to large distortions and the generation of small scales. The mean motions of the secondary ring occur on a relatively slow time scale which can be characterized by R_2/V_0 (the time required to propagate one radius R_2 at the instantaneous mean velocity V_0). This mean motion can be decoupled from the instability dynamics which occur on a relatively fast time scale $1/\sigma$ (where σ is the instability growth rate), since $\sigma R_2/V_0 \gg 1$.

The dynamics were modelled by two inviscid vortex rings in the presence of their images (inviscid boundary). Figure 11 shows a schematic of the problem formulation. The subscripts 1, 2, 3 and 4 correspond to the primary ring, the secondary ring, the primary-ring image, and the secondary-ring image, respectively. Simulation results suggest that viscous effects (while helping to fix the primary-ring position) only weakly modify the secondary ring motions. Inclusion of the wall boundary layer has a negligible effect since it is in such close proximity to its image. The vortex cores were approximated by uniform distributions of vorticity. The secondary-ring-core radius a_2 was assumed to be small relative to the ring radius R_2, and relative to the instability wavelength $2\pi R_2/n$ (n is the azimuthal mode number); this is in accordance with the long-wavelength approximation. These assumptions lead to an asymptotic approximation for the core characteristics, but they also introduce a limit on the number of azimuthal modes for which the analysis will be valid, $na_2/R_2 \ll 1$ (Widnall *et al.*

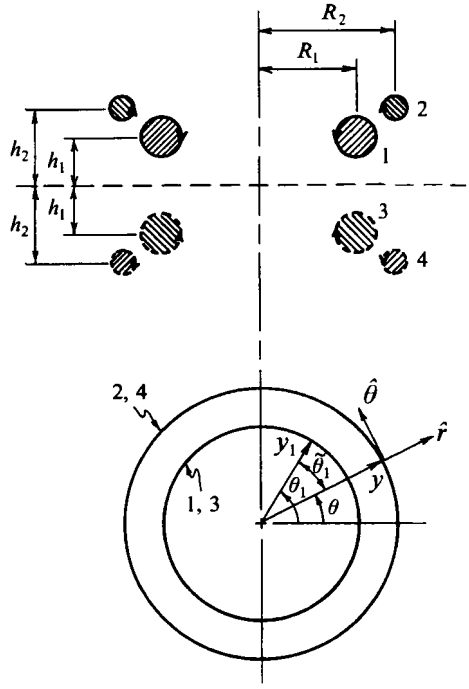

FIGURE 11. Schematic of the vortex-ring model considered in the analysis.

1974; Moore & Saffman 1974). However, comparisons between the exact and asymptotic dispersion relations for waves on a vortex filament show good quantitative agreement for $na_2/R_2 \approx 1$ (Widnall *et al.* 1974). For larger values of na_2/R_2 the asymptotic result predicts spurious instabilities. In the present analysis, the instability is driven by the presence of the primary ring so the results are relatively insensitive to the secondary-ring-core characteristics. When comparing to numerical results the effective core size, determined quantitatively from the simulations as shown in figure 8(*b*), was used.

The instability evolution is described by a sequence of 'local' stability calculations under a quasi-steady assumption. The mean position of the secondary ring was temporarily considered fixed while the local growth rate was calculated. This is justified by the relatively small change in the mean position as compared to the instability growth. The stability analysis follows the earlier work of Widnall & Sullivan (1973) in which they investigated the stability of an isolated vortex ring propagating freely through a fluid.

The perturbation in the secondary ring was taken to be an azimuthally periodic displacement in both the radial ρ and axial ζ directions. These displacements result in induced velocities which can either amplify or damp the initial perturbations. The ring positions are referenced to a coordinate system which moves with the mean axial velocity of the secondary ring. A position vector $\boldsymbol{y}$ is introduced to describe the location on the secondary ring where the induced velocity was calculated

$$\boldsymbol{y} = (R_2 + \rho e^{in\theta})\hat{\boldsymbol{r}} + (\zeta e^{in\theta})\hat{\boldsymbol{z}}. \tag{4.1}$$

The unit vectors $\hat{\boldsymbol{r}}$, $\hat{\boldsymbol{\theta}}$ and $\hat{\boldsymbol{z}}$ correspond to the local radial, azimuthal and axial directions, respectively. The induced velocity at $\boldsymbol{y}$ results from the primary ring represented by the vector

$$y_1 = (R_1 \cos\tilde{\theta}_1)\hat{r} + (R_1 \sin\tilde{\theta}_1)\hat{\theta} - (h_2 - h_1)\hat{z}, \tag{4.2}$$

the self-induction of the secondary ring represented by the vector

$$y_2 = (R_2 + \rho e^{in\theta_2})\cos\tilde{\theta}_2 \hat{r} + (R_2 + \rho e^{in\theta_2})\sin\tilde{\theta}_2 \hat{\theta} + (\zeta e^{in\theta_2})\hat{z}, \tag{4.3}$$

and the two image rings represented by the vectors

$$y_3 = (R_1 \cos\tilde{\theta}_3)\hat{r} + (R_1 \sin\tilde{\theta}_3)\hat{\theta} - (h_1 + h_2)\hat{z}, \tag{4.4}$$

$$y_4 = (R_2 + \rho e^{in\theta_4})\cos\tilde{\theta}_4 \hat{r} + (R_2 + \rho e^{in\theta_4})\sin\tilde{\theta}_4 \hat{\theta} + (-2h_2 + \zeta e^{in\theta_4})\hat{z}. \tag{4.5}$$

The angles θ_i $(i = 1, 4)$ correspond to the azimuthal positions of the vectors y_i; $\tilde{\theta}_i$ provides the relative angle between θ and θ_i, $\tilde{\theta}_i = \theta_i - \theta$. These vectors are shown schematically in figure 11.

From the Biot–Savart law, the total induced velocity at y resulting from both rings (and their images) is given by

$$q(y) = q_1(y) + q_2(y) + q_3(y) + q_4(y), \tag{4.6a}$$

where

$$q_i(y) = \frac{\Gamma_i}{4\pi}\int_{C_i} \frac{(y_i - y)}{|y_i - y|^3} \times dy_i. \tag{4.6b}$$

C_i is a contour around the ith ring and Γ_i is the circulation of the ith ring. The induced velocities q_1, q_3 and q_2, q_4 result from the primary and secondary rings, respectively. When y_2 is close to y, details of the secondary-ring vortex core were used to estimate the local induction. Substituting y and y_i $(i = 1, 4)$ into (4.6) leads to general expressions for the induced velocities:

$$q_i(y) = U_{0i}\hat{r} + V_{0i}\hat{z} + (\zeta e^{in\theta} U_{\zeta i} + \rho e^{in\theta} U_{\rho i})\hat{r} + (\zeta e^{in\theta} V_{\zeta i} + \rho e^{in\theta} V_{\rho i})\hat{z}, \quad i = 1, 3, 4, \tag{4.7}$$

$$q_2(y) = V_{02}\hat{z} + (\zeta e^{in\theta} U_{\zeta 2})\hat{r} + (\rho e^{in\theta} V_{\rho 2})\hat{z}, \tag{4.8}$$

where U and V are the radial and axial components, respectively. Integrals defining the various velocity components of (4.7) and (4.8) are given in the Appendix. The first subscript on the velocity components signifies the secondary-ring 'source' perturbation (i.e. 0 for mean quantities, ρ for radial perturbations, or ζ for axial perturbations). The second subscript identifies which ring provides the induction. The secondary-ring self-induction velocity q_2 is identical to the expression derived by Widnall & Sullivan (1973) for the long-wavelength stability of an isolated ring.

4.2. *Stability characteristics*

The induced motion of the secondary vortex ring satisfies a kinematic equation derived from the temporally varying position vector. In the absence of any constraints on the ring motion,

$$\frac{dy_F}{dt} = \frac{dy}{dt} + V_0\hat{z} = q(y), \tag{4.9}$$

where y_F is the position measured from a fixed reference frame and V_0 is the mean axial velocity of the secondary ring. Differentiating (4.1) with respect to t yields

$$\frac{dy}{dt} = \left(\frac{dR_2}{dt} + \frac{d\rho}{dt}e^{in\theta}\right)\hat{r} + \frac{d\zeta}{dt}e^{in\theta}\hat{z}. \tag{4.10}$$

On combining (4.6)–(4.10) the mean velocities for the secondary ring become

$$U_0 = \frac{\mathrm{d}R_2}{\mathrm{d}t} = U_{01} + U_{03} + U_{04}, \tag{4.11}$$

$$V_0 = V_{01} + V_{02} + V_{03} + V_{04}. \tag{4.12}$$

The instability amplitudes are governed by

$$\frac{\mathrm{d}\rho}{\mathrm{d}t} = \rho U_\rho + \zeta U_\zeta, \tag{4.13}$$

$$U_\rho = U_{\rho 1} + U_{\rho 3} + U_{\rho 4}, \quad U_\zeta = U_{\zeta 1} + U_{\zeta 2} + U_{\zeta 3} + U_{\zeta 4},$$

$$\frac{\mathrm{d}\zeta}{\mathrm{d}t} = \rho V_\rho + \zeta V_\zeta, \tag{4.14}$$

$$V_\rho = V_{\rho 1} + V_{\rho 2} + V_{\rho 3} + V_{\rho 4}, \quad V_\zeta = V_{\zeta 1} + V_{\zeta 3} + V_{\zeta 4}.$$

These equations describe the growth or decay of disturbances for a given position of the secondary vortex ring. In general, the mean position of the secondary ring (and thus U_ρ, U_ζ, V_ρ, and V_ζ) varies slowly with time and (4.13) and (4.14) are non-autonomous. The equation parameters also depend on the ring circulations and the secondary-ring-core characteristics.

Three different approaches for solving (4.13) and (4.14) were considered. In the first approach, the stability equations were simultaneously integrated with the corresponding equations for the mean position. This provides a completely analytical solution, requiring only initial values for the mean position and the disturbance amplitudes. In the second approach, (4.13) and (4.14) were integrated for the disturbance evolution, but the mean positions derived from the numerical simulations were used. This has the advantage of separating the stability results from the mean position results when comparing to the simulations.

In the third approach, the variations of U_ρ, U_ζ, V_ρ and V_ζ were neglected and it was assumed that the two components of the ring perturbation have solutions of the form

$$\rho(t) = \rho_0 \mathrm{e}^{\sigma t}, \quad \zeta(t) = \zeta_0 \mathrm{e}^{\sigma t}. \tag{4.15}$$

This leads to a characteristic growth rate for the total perturbation $\xi = (\rho^2 + \zeta^2)^{1/2}$. The real part of σ gives the temporal growth for ξ and the imaginary part gives the frequency for oscillations around the mean position. Substituting (4.15) into (4.13) and (4.14) and imposing the solvability condition yields

$$\sigma = \tfrac{1}{2}(U_\rho + V_\zeta) \pm \tfrac{1}{2}[(U_\rho + V_\zeta)^2 - 4(U_\rho V_\zeta - U_\zeta V_\rho)]^{1/2}. \tag{4.16}$$

This provides a simple demarcation for the onset of instability. In the absence of the primary and image rings, $U_\rho = V_\zeta = 0$ and $U_\zeta = U_{\zeta 2}$, $V_\rho = V_{\rho 2}$. Equation (4.16) then reduces to

$$\sigma = [U_{\zeta 2} V_{\rho 2}]^{1/2},$$

in agreement with Widnall & Sullivan (1973).

When focusing on the characteristic growth rate, the instability can be described in terms of the dimensionless quantities $\bar{\Gamma} = \Gamma_1/\Gamma_2$, $\bar{a}_2 = a_2/R_2$, $\bar{R} = R_1/R_2$, $\bar{h}_1 = h_1/R_2$, and $\bar{h}_2 = h_2/R_2$. An instability growth-rate parameter $\bar{\sigma}$ can then be expressed as

$$\bar{\sigma}(\bar{\Gamma}, \bar{a}_2, \bar{R}, \bar{h}_1, \bar{h}_2; n) = \sigma 4\pi R_2^2/\Gamma_2.$$

For fixed ring positions and fixed secondary-ring characteristics, $\bar{\sigma}$ depends only on the relative circulation $\bar{\Gamma}$ and the mode number n. When $\bar{\Gamma} = 0$, $\bar{\sigma}$ is purely imaginary for

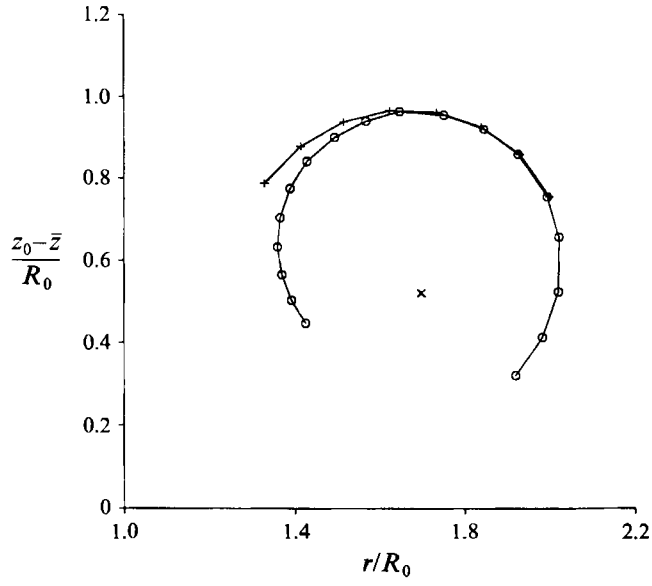

FIGURE 12. Secondary-ring mean trajectory as predicted by the analysis (+) and from the numerical simulation (○). The primary-ring position (r_1, z_1) used in the analysis is given by (×).

all modes (i.e. perturbations oscillate without growth or decay). As $\bar{\Gamma}$ is increased, the different modes – starting with $n = 1$ – become unstable; the value of $\bar{\Gamma}$ at the onset of instability for each mode will depend on the parameters $\bar{a}_2$, $\bar{R}$, $\bar{h}_1$, $\bar{h}_2$.

4.3. *Analytical results*

In this analysis, the primary- and secondary-ring circulations and the secondary-ring-core characteristics were taken to be constant. Values for these parameters are extracted from the numerical simulations as described in §3. Calculations for the mean propagation of the secondary ring are shown in figure 12. The trajectories were calculated using (4.11) and (4.12) with parameter values $\Gamma_1 = -4$, $\Gamma_2 = 1.14$, and $a_2 = 0.18$ corresponding to the simulation results of figures 6 and 8. Numerical results are presented for comparison. The time step between data points, $\Delta t = 0.1$, is the same for the analysis and simulation. The initial ring position for the analysis was chosen to match the simulation at $t = 3.0$. At this time the secondary ring first becomes 'distinguished' from the vorticity on the wall and the primary-ring position becomes almost fixed. The location (r_1, z_1) signifies the fixed position of the primary ring used in the analysis. The trajectories from the two methods are in good agreement from $t = 3.0$ to 3.4. The most significant difference after $t = 3.3$ is the rate of propagation along the trajectory, rather than the shape of the trajectory. These differences can be traced to viscous and non-uniform core effects, not accounted for in the analysis. Simulations for different flow conditions show a departure from inviscid ring-propagation rates as the level of viscous decay or ring-core distortion is increased.

To calculate the evolution of the instabilities, (4.13) and (4.14) were integrated with the parameter values used in figure 12. In the first instance, the case where U_ρ, U_ξ, V_ρ, and V_ξ were determined from the mean trajectories calculated using (4.11) and (4.12) is considered. Figure 13(*a*) shows the amplitude evolutions for $n = 6$ calculated from the model in conjunction with the numerical simulation results. The initial amplitudes were chosen to match the numerical values at $t = 3.0$. The radial position at $t = 3.0$ is

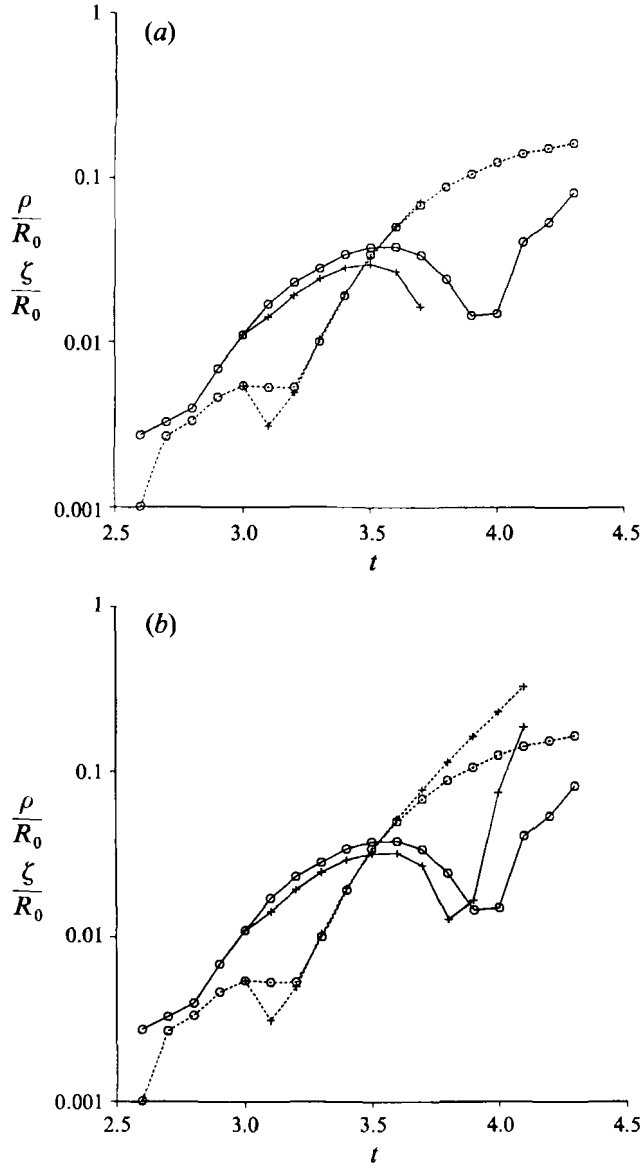

FIGURE 13. Evolution of the secondary-ring instability amplitudes ρ (solid) and ζ (dashed) as predicted by the analysis (+) and the numerical simulation (○). (*a*) Analysis based on analytical mean trajectories, (*b*) analysis based on numerical simulation mean trajectories.

$R_2 = 2.0$ which gives $na_2/R_2 \approx 0.54$. The amplitude curves show an initial growth in ρ while ζ is being damped. This is followed by a rapid growth in ζ and an eventual decay of ρ. The amplitude curves from the analysis are in good agreement with the simulation results. The increasing deviations for the ρ amplitude beyond $t \approx 3.5$ are the result of differences in the mean trajectories.

The amplitude curves calculated using values of U_ρ, U_ζ, V_ρ, and V_ζ that were determined from the numerical-simulation mean trajectories are now considered. Using the numerical mean trajectories permits the calculation of the amplitude curves at larger times where the analytical trajectories show significant deviations from the

simulations. Figure 13(*b*) shows the amplitude evolutions for $n = 6$ calculated from the model in conjunction with the numerical simulation results. The amplitude curves from the analysis are in good agreement with the simulation results up to $t \approx 3.7$. Beyond $t \approx 3.7$ the curves continue to be in qualitative agreement. The large differences at $t = 4.0$ are likely the result of nonlinear effects (figure 9 shows that the amplitudes at $t \approx 4.0$ are $O(1)$). The good agreement between the analytical and numerical results suggests that the analytical model contains the essential features that drive the instability of the secondary ring.

Analytical predictions for the growth-rate parameter σ are also in reasonable agreement with the simulation results. For the simulation result of figure 10, the growth rate for the combined amplitude ξ at $t = 3.1$ is $\sigma \approx 2.8$. Using (4.16) for the same conditions, the analysis gives a growth rate of $\sigma = 3.5$. This difference can easily be attributed to the additional assumptions that went into deriving (4.16) from (4.13) and (4.14), most significantly the assumption that ρ and ζ evolve with the same growth rate.

In the absence of the primary ring, the thin-core secondary ring would be stable to small perturbations. The primary ring induces a strain across the core of the secondary ring. When this strain field is of sufficient magnitude, it amplifies the secondary-ring perturbation through vortex tilting and stretching similar to the secondary-instability mechanism in shear flows (Orszag & Patera 1983; Herbert 1983). The perturbation induces a rotation which, in the presence of strain, leads to vortex stretching. The stretching amplifies the perturbation and enhances the rotation. This process leads to very rapid growth of the instability. Additionally, Smith *et al.* (1991) showed that the means by which a three-dimensional disturbance to a vortex filament spreads and grows is the result of the nonlinear interaction between the vortex and the background strain, with the amplification strongly dependent on the level of this strain. A similar mechanism is responsible here except that the strain is associated with the presence of the primary vortex ring rather than with the background mean strain.

5. Conclusions

The flow associated with a vortex ring impacting a solid boundary was investigated by numerically solving the full Navier–Stokes equations. The essential dynamics of this process had been identified earlier in experimental studies. The numerical results show good qualitative agreement with the experiments and also provide access to the quantitative details of the flow. As the vortex ring approaches the solid boundary, a secondary vortex ring is generated. The secondary ring propagates around the initial (primary) ring due to the combined influence of the primary- and secondary-ring inductions. One of the key features observed in experiments and in the numerical simulations is the development of an instability in the secondary vortex ring. This instability leads to a breakup of the secondary vortex, giving rise to smaller-scale coherent motions.

The dynamics of the instability were further investigated by developing an analytical model for the evolution of the secondary ring. The analysis was based on quasi-steady and long-wavelength approximations. The instability of the secondary ring is governed by a pair of coupled ordinary differential equations. These equations describe the temporal evolution of the axial and radial components of the instability. Comparisons between the analysis and simulation show good agreement for the early development of the instability. The instability of the secondary ring is the result of vortex stretching and tilting in the presence of the primary-ring strain field. The strength of the

instability depends on the ratio of the primary- and secondary-ring circulations and on the position of the secondary ring relative to the primary. For the conditions of the numerical simulations, strong instability growth is observed. This is in contrast to the isolated thin-core vortex ring, which is stable to long-wavelength perturbations.

This work was supported by the Naval Research Laboratory under the Fluid Dynamics Task Area and a Cray 6.1 grant. The authors also gratefully acknowledge the assistance of Nadim Nakhleh and Michael McMullin in creating the colour figures.

Appendix

The induced velocities resulting from the primary ring and its image $i = 1, 3$ are given by

$$U_{0i} = \frac{\Gamma_i}{4\pi}\int_{-\pi}^{\pi} G_1^{-3/2} h R_1 \cos\tilde{\theta}_1 \,\mathrm{d}\tilde{\theta}_1, \tag{A 1}$$

$$V_{0i} = \frac{\Gamma_i}{4\pi}\int_{-\pi}^{\pi} G_1^{-3/2} R_1 (R_1 - R_2\cos\tilde{\theta}_1)\,\mathrm{d}\tilde{\theta}_1, \tag{A 2}$$

$$U_{\rho i} = \frac{\Gamma_i}{4\pi}\int_{-\pi}^{\pi} -3G_1^{-5/2}(hR_1 R_2\cos\tilde{\theta}_1 - hR_1^2\cos^2\tilde{\theta}_1)\,\mathrm{d}\tilde{\theta}_1, \tag{A 3}$$

$$U_{\zeta i} = \frac{\Gamma_i}{4\pi}\int_{-\pi}^{\pi} (G_1^{-3/2} R_1\cos\tilde{\theta}_1 - 3G_1^{-5/2} h^2 R_1\cos\tilde{\theta}_1)\,\mathrm{d}\tilde{\theta}_1, \tag{A 4}$$

$$V_{\rho i} = \frac{\Gamma_i}{4\pi}\int_{-\pi}^{\pi} (-G_1^{-3/2} R_1\cos\tilde{\theta}_1 - 3G_1^{-5/2} R_1 (R_2 - R_1\cos\tilde{\theta}_1)(R_1 - R_2\cos\tilde{\theta}_1))\,\mathrm{d}\tilde{\theta}_1, \tag{A 5}$$

$$V_{\zeta i} = \frac{\Gamma_i}{4\pi}\int_{-\pi}^{\pi} -3G_1^{-5/2} h R_1 (R_1 - R_2\cos\tilde{\theta}_1)\,\mathrm{d}\tilde{\theta}_1, \tag{A 6}$$

where

$$G_1 = R_1^2 + R_2^2 - 2R_1 R_2\cos\tilde{\theta}_1 + h^2, \tag{A 7}$$

with $h = h_2 - h_1$ for $i = 1$, $h = h_2 + h_1$ for $i = 3$, and $\Gamma_3 = -\Gamma_1$.

The induced velocities resulting from the secondary-ring self-interaction $i = 2$ are given by

$$V_{02} = \frac{\Gamma_2}{4\pi}\int_{-\pi}^{\pi} G_2^{-3/2} R_2^2 (1 - \cos\tilde{\theta}_2)\,\mathrm{d}\tilde{\theta}_2, \tag{A 8}$$

$$U_{\zeta 2} = \frac{\Gamma_2}{4\pi}\int_{-\pi}^{\pi} G_2^{-3/2} R_2 (\mathrm{e}^{\mathrm{i}n\tilde{\theta}_2}\mathrm{i}n\sin\tilde{\theta}_2 + (1 - \mathrm{e}^{\mathrm{i}n\tilde{\theta}_2})\cos\tilde{\theta}_2)\,\mathrm{d}\tilde{\theta}_2, \tag{A 9}$$

$$V_{\rho 2} = \frac{\Gamma_2}{4\pi}\int_{-\pi}^{\pi} G_2^{-3/2} R_2 (\mathrm{e}^{\mathrm{i}n\tilde{\theta}_2} - \cos\tilde{\theta}_2 - \mathrm{i}n\,\mathrm{e}^{\mathrm{i}n\tilde{\theta}_2}\sin\tilde{\theta}_2 + \mathrm{e}^{\mathrm{i}n\tilde{\theta}_2}(1 - \cos\tilde{\theta}_2) - \tfrac{3}{2}(1 + \mathrm{e}^{\mathrm{i}n\tilde{\theta}_2})(1 - \cos\tilde{\theta}_2))\,\mathrm{d}\tilde{\theta}_2, \tag{A 10}$$

where

$$G_2 = 2R_2^2(1 - \cos\tilde{\theta}_2). \tag{A 11}$$

The induced velocities resulting from the secondary-ring image $i = 4$ are given by

$$U_{04} = \frac{-\Gamma_2}{4\pi}\int_{-\pi}^{\pi} G_4^{-3/2} h R_2 \cos\tilde{\theta}_4 \,\mathrm{d}\tilde{\theta}_4, \tag{A 12}$$

$$V_{04} = \frac{-\Gamma_2}{4\pi}\int_{-\pi}^{\pi} G_4^{-3/2} R_2^2 (1-\cos\tilde{\theta}_4)\,\mathrm{d}\tilde{\theta}_4, \tag{A 13}$$

$$U_{\rho 4} = \frac{-\Gamma_2}{4\pi}\int_{-\pi}^{\pi} (G_4^{-3/2} h\,\mathrm{e}^{\mathrm{i}n\tilde{\theta}_4}(\cos\tilde{\theta}_4 + \mathrm{i}n\sin\tilde{\theta}_4) - 3G_4^{-5/2} h R_2^2 \cos\tilde{\theta}_4 (1+\mathrm{e}^{\mathrm{i}n\tilde{\theta}_4})(1-\cos\tilde{\theta}_4))\,\mathrm{d}\tilde{\theta}_4, \tag{A 14}$$

$$U_{\zeta 4} = \frac{-\Gamma_2}{4\pi}\int_{-\pi}^{\pi} (G_4^{-3/2} R_2 (\cos\tilde{\theta}_4(1-\mathrm{e}^{\mathrm{i}n\tilde{\theta}_4}) + \mathrm{i}n\,\mathrm{e}^{\mathrm{i}n\tilde{\theta}_4}\sin\tilde{\theta}_4) - 3G_4^{-5/2} h^2 R_2 \cos\tilde{\theta}_4 (1-\mathrm{e}^{\mathrm{i}n\tilde{\theta}_4}))\,\mathrm{d}\tilde{\theta}_4, \tag{A 15}$$

$$V_{\rho 4} = \frac{-\Gamma_2}{4\pi}\int_{-\pi}^{\pi} (G_4^{-3/2} R_2 (2\,\mathrm{e}^{\mathrm{i}n\tilde{\theta}_4} - \cos\tilde{\theta}_4(1+\mathrm{e}^{\mathrm{i}n\tilde{\theta}_4}) - \mathrm{i}n\,\mathrm{e}^{\mathrm{i}n\tilde{\theta}_4}\sin\tilde{\theta}_4) - 3G_4^{-5/2} R_2^3 (1-\cos\tilde{\theta}_4)^2 (1+\mathrm{e}^{\mathrm{i}n\tilde{\theta}_4}))\,\mathrm{d}\tilde{\theta}_4, \tag{A 16}$$

$$V_{\zeta 4} = \frac{-\Gamma_2}{4\pi}\int_{-\pi}^{\pi} -3G_4^{-5/2} h R_2^2 (1-\cos\tilde{\theta}_4)(1-\mathrm{e}^{\mathrm{i}n\tilde{\theta}_4})\,\mathrm{d}\tilde{\theta}_4, \tag{A 17}$$

where

$$G_4 = 2R_2^2(1-\cos\tilde{\theta}_4) + h^2, \tag{A 18}$$

with $h = 2h_2$.

The integrals for $i = 1, 3, 4$ are evaluated numerically for given ring positions and ring characteristics. In evaluating the integrals for $i = 2$, the integrands become singular when $\tilde{\theta}_2 = 0$. However, these integrals can be evaluated by accounting for the finite size of the secondary-ring core. Our results are based on the asymptotic local-induction approximation used by Widnall & Sullivan (1973).

REFERENCES

ACALAR, M. S. & SMITH, C. R. 1987 A study of hairpin vortices in a laminar boundary layer. Part 2. Hairpin vortices generated by fluid injection. *J. Fluid Mech.* **175**, 43–83.

BERNAL, L. P. & KWON, J. T. 1989 Vortex ring dynamics at a free surface. *Phys. Fluids* A **1**, 449–451.

BERNARD, P. S., THOMAS, J. T. & HANDLER, R. A. 1993 Vortex dynamics and the production of Reynolds stress. *J. Fluid Mech.* **253**, 385–419.

BROOKE, J. W. & HANRATTY, T. J. 1993 Origin of turbulence-producing eddies in a channel flow. *Phys. Fluids* A **5**, 1011–1022.

CANTWELL, B. J. 1986 Viscous starting jets. *J. Fluid Mech.* **173**, 159–189.

CERRA, A. W. & SMITH, C. R. 1983 Experimental observations of vortex ring interaction with the fluid adjacent to a surface. *Rep.* FM-4. Department of Mechanical Engineering and Mechanics, Leigh University, Bethlehem, PA.

CHU, C. C. & FALCO, R. E. 1988 Vortex ring/viscous wall layer interaction model of the turbulence production process near walls. *Exps. Fluids* **6**, 305–315.

DOLIGALSKI, T. L., SMITH, C. R. & WALKER, J. D. A. 1994 Vortex interaction with walls. *Ann. Rev. Fluid Mech.* **26**, 573–616.

DOMMERMUTH, D. G. 1993 The laminar interaction of a pair of vortex tubes with a free surface. *J. Fluid Mech.* **246**, 91–115.

FALCO, R. E. 1991 A coherent structure model of the turbulent boundary layer and its ability to predict Reynolds number dependence. *Phil. Trans. R. Soc. Lond.* A **336**, 103–129.

GOLDSTEIN, D., HANDLER, R. & SIROVICH, L. 1993 Modeling a no-slip flow boundary with an external force field. *J. Comput. Phys.* **105**, 354–366.

GOTTLEIB, D. & ORSZAG, S. A. 1977 *Numerical Analysis of Spectral Methods: Theory and Applications.* CBMS-NSF, Society for Industrial and Applied Mathematics. Philadelphia, PA, USA.

HERBERT, TH. 1983 Secondary instability of plane channel flow to subharmonic three-dimensional disturbances. *Phys. Fluids* **26**, 871–874.

KIM, J., MOIN, P. & MOSER, R. 1987 Turbulence statistics in fully developed channel flow at low Reynolds number. *J. Fluid Mech.* **177**, 133–166.

LIM, T. T. 1989 An experimental study of a vortex ring interacting with an inclined wall. *Exps. Fluids* **7**, 453–463.

MAGARVEY, R. H. & MACLATCHY, C. S. 1964*a* The formation and structure of vortex rings. *Can. J. Phys.* **42**, 678–683.

MAGARVEY, R. H. & MACLATCHY, C. S. 1964*b* The disintegration of vortex rings. *Can. J. Phys.* **42**, 684–689.

MAXWORTHY, T. 1972 The structure and stability of vortex rings. *J. Fluid Mech.* **51**, 15–32.

MCCORMACK, P. D. & CRANE, L. 1973 *Physical Fluid Dynamics.* Academic.

MOORE, D. W. & SAFFMAN, P. G. 1974 A note on the stability of a vortex ring of small cross-section. *Proc. R. Soc. Lond.* A **338**, 535–537.

ORLANDI, P. 1990 Vortex dipole rebound from a wall. *Phys. Fluids* A **2**, 1429–1436.

ORLANDI, P. & VERZICCO, R. 1993 Vortex rings interacting with walls: axisymmetric and three-dimensional simulations. *J. Fluid Mech.* **256**, 615–646.

ORSZAG, S. A. & PATERA, A. T. 1981 Subcritical transition to turbulence in planar shear flows. In *Transition and Turbulence* (ed. R. E. Meyer), pp. 127–146. Academic.

ORSZAG, S. A. & PATERA, A. T. 1983 Secondary instability of wall-bounded shear flows. *J. Fluid Mech.* **128**, 347–385.

ROBINSON, S. K. 1989 A review of vortex structures and associated coherent motions in turbulent boundary layers. In *Proc. Second IUTAM Symp. on Structure of Turbulence and Drag Reduction.* Zurich.

ROBINSON, S. K. 1991 Coherent motions in the turbulent boundary layer. *Ann. Rev. Fluid Mech.* **23**, 601–639.

SAFFMAN, P. G. 1975 On the formation of vortex rings. *Stud. Appl. Maths.* **54**, 261–268.

SAFFMAN, P. G. 1978 The number of waves on unstable vortex rings. *J. Fluid Mech.* **84**, 625–639.

SALLET, D. W. & WIDMAYER, R. S. 1974 An experimental investigation of laminar and turbulent vortex rings in air. *Z. Flugwiss.* **22**, 207–215.

SARPKAYA, T. & SUTHON, P. B. 1991 Scarred and striated signature of a vortex pair on the free surface. In *Proc. Eighteenth Symp. on Naval Hydrodyn., University of Michigan, 19–24 August 1990*, pp. 503–518. National Academy.

SMITH, C. R., WALKER, J. D. A., HAIDARI, A. H. & SOBRUN, U. 1991 On the dynamics of near-wall turbulence. *Phil. Trans. R. Soc. Lond.* A **336**, 134–175.

SWEARINGEN, J. D., CROUCH, J. D. & HANDLER, R. A. 1991 Stability aspects of vortex ring/wall interaction. *Bull. Am. Phys. Soc.* **36**, 2661.

WALKER, J. D. A., SMITH, C. R., CERRA, A. W. & DOLIGALSKI, T. L. 1987 The impact of a vortex ring on a wall. *J. Fluid Mech.* **181**, 99–140.

WIDNALL, S. E., BLISS, D. B. & TSAI, C. Y. 1974 The instability of short waves on a vortex ring. *J. Fluid Mech.* **66**, 35–47.

WIDNALL, S. E. & SULLIVAN, J. P. 1973 On the stability of vortex rings. *Proc. R. Soc. Lond.* A **332**, 335–353.

WILLMARTH, W. W., TRYGGVASON, G., HIRSA, A. & YU, D. 1989 Vortex pair generation and interaction with a free surface. *Phys. Fluids* A **1**, 170–172.

YAMADA, H. & MATSUI, T. 1982 Visualization of vortex interaction using smoke-wire technique. In *Flow Visualization II* (ed. W. Merzkirch), pp. 355–359. Hemisphere.